

# Can conduction induce convection? The non-linear saturation of buoyancy instabilities in dilute plasmas

Michael McCourt,<sup>1\*</sup> Ian J. Parrish,<sup>1,2</sup> Prateek Sharma<sup>1,2</sup> & Eliot Quataert<sup>1</sup>

<sup>1</sup>*Department of Astronomy and Theoretical Astrophysics Center, University of California Berkeley, Berkeley, CA 94720*

<sup>2</sup>*Einstein Fellow*

Submitted to MNRAS, ?, 2010

## ABSTRACT

We study the effects of anisotropic thermal conduction on low-collisionality, astrophysical plasmas using two and three-dimensional magnetohydrodynamic simulations. For weak magnetic fields, dilute plasmas are buoyantly unstable for either sign of the temperature gradient: the heat-flux-driven buoyancy instability (HBI) operates when the temperature increases with radius while the magnetothermal instability (MTI) operates in the opposite limit. In contrast to previous results, we show that, in the presence of a sustained temperature gradient, the MTI drives strong turbulence and operates as an efficient magnetic dynamo (akin to standard, adiabatic convection). Together, the turbulent and magnetic energies contribute up to  $\sim 10\%$  of the pressure support in the plasma. In addition, the MTI drives a large convective heat flux,  $\sim 1.5\% \times \rho c_s^3$ . These findings are robust even in the presence of an external source of strong turbulence. Our results on the nonlinear saturation of the HBI are consistent with previous studies but we explain physically why the HBI saturates quiescently by re-orienting the magnetic field (suppressing the conductive heat flux through the plasma), while the MTI saturates by generating sustained turbulence. We also systematically study how an external source of turbulence affects the saturation of the HBI: such turbulence can disrupt the HBI only on scales where the shearing rate of the turbulence is faster than the growth rate of the HBI. In particular, our results provide a simple mapping between the level of turbulence in a plasma and the effective isotropic thermal conductivity. We discuss the astrophysical implications of these findings, with a particular focus on the intracluster medium of galaxy clusters.

**Key words:** conduction, convection, instabilities, MHD, turbulence — galaxies: clusters: general

## 1 INTRODUCTION

The thermodynamics of a plasma can have dramatic and sometimes unexpected implications for its dynamical evolution. For example, thermal conduction can reduce the accretion rate in spherical accretion flows by as much as two to three orders of magnitude relative to the Bondi value (Johnson & Quataert 2007; Shcherbakov & Baganoff 2010). More relevant to this paper, Balbus (2000) and Quataert (2008) demonstrated that the convective dynamics of conducting

plasmas are completely different from those of an adiabatic fluid. This paper focuses on the nonlinear evolution and saturation of this convection.

When anisotropic conduction is rapid compared to the dynamical response of a plasma, the temperature gradient, rather than the entropy gradient, determines the plasma's convective stability. The convective instability in this limit is known as the heat-flux-driven buoyancy instability (HBI) when the temperature increases with height ( $\mathbf{g} \cdot \nabla T < 0$ ) or the magnetothermal instability (MTI) when the temperature decreases with height ( $\mathbf{g} \cdot \nabla T > 0$ ). We summarize the linear physics of these instabilities in section 2. Parrish & Stone

\* E-mail: mkmcc@astro.berkeley.edu

(2005, 2007) and Parrish & Quataert (2008) studied the nonlinear development of the MTI and HBI using numerical simulations. These instabilities couple the magnetic structure of the plasma to its thermal properties and potentially have important implications for galaxy clusters (Parrish et al. 2008, 2009; Bogdanović et al. 2009; Sharma et al. 2009a; Parrish et al. 2010; Bogdanović et al. 2010; Ruszkowski & Oh 2010), hot accretion flows onto compact objects (Sharma et al. 2008), and the interiors and surface layers of white dwarfs and neutron stars (Chang et al. 2010).

In this paper, we revisit the nonlinear behavior of the HBI and MTI. We focus on the physics of their saturation, but also include a lengthy discussion of possible astrophysical implications in section 6. Our analysis is idealized (we use a plane-parallel approximation and neglect radiative cooling), but we are able to understand the nonlinear behavior of the HBI and MTI, and therefore their astrophysical implications, more thoroughly than in previous papers. Our results for the saturation of the HBI are similar to those of Parrish & Quataert (2008), but with an improved understanding of the saturation mechanism. Our results for the MTI, however, differ from previous results, significantly changing the predicted astrophysical implications of the MTI. We show in section 4.2 that this is because the development of the MTI in many previous simulations has been hindered by the finite size of the simulation domain.

The structure of this paper is as follows. We describe the linear physics of the MTI and HBI in section 2. We describe our computational setup in section 3 and the results of our numerical simulations in section 4. In order to better understand how the saturation of the HBI and MTI may change in a more realistic astrophysical environment, we study the interaction between these instabilities and an external source of turbulence or fluid motion (section 5). Finally, in section 6, we summarize our results and discuss the astrophysical implications of our work.

## 2 BACKGROUND

### 2.1 Equations and Assumptions

We assume that the plasma is an ideal gas with an adiabatic index  $\gamma = 5/3$  and model it using the magneto-hydrodynamic (MHD) equations, neglecting all dissipative processes except thermal conduction. In Cartesian coordinates, the equations for the conservation of mass, momentum and magnetic flux, and for the evolution of internal energy are

$$\frac{\partial \rho}{\partial t} + \nabla \cdot (\rho \mathbf{v}) = 0, \quad (1a)$$

$$\frac{\partial}{\partial t} (\rho \mathbf{v}) + \nabla \cdot \left[ \rho \mathbf{v} \otimes \mathbf{v} + \left( P + \frac{B^2}{8\pi} \right) \mathbf{I} + \frac{\mathbf{B} \otimes \mathbf{B}}{4\pi} \right] = \rho (\mathbf{g} + \mathbf{f}), \quad (1b)$$

$$\frac{\partial \mathbf{B}}{\partial t} = \nabla \times (\mathbf{v} \times \mathbf{B}), \quad (1c)$$

$$\rho T \frac{ds}{dt} = -\nabla \cdot \mathbf{Q}_{\text{cond}}, \quad (1d)$$

where  $\rho$  is the mass density,  $\mathbf{v}$  is the fluid velocity,  $\otimes$  denotes a tensor product,  $P$  is the pressure,  $\mathbf{B}$  is the magnetic field,  $\mathbf{I}$  is the unit matrix,  $\mathbf{g}$  is the gravitational field,  $\mathbf{f}$  is an externally imposed force,  $T$  is the temperature,

$$s = \frac{1}{\gamma - 1} \frac{k_B}{m_H} \ln \left( \frac{P}{\rho^\gamma} \right) \quad (2)$$

is the entropy per unit mass,  $d/dt = \partial/\partial t + \mathbf{v} \cdot \nabla$  is the Lagrangian time derivative, and  $\mathbf{Q}_{\text{cond}}$  is the conductive heat flux.

We ignore the ion contribution to the conductive heat flux, which is smaller than the electron contribution by a factor of  $(m_i/m_e)^{1/2} \approx 42$ . We assume that the electrons have mean free paths much longer than their gyro-radii (as is the case in the intracluster medium (ICM) of galaxy clusters); the electrons therefore move almost entirely along magnetic field lines. Consequently, the thermal conductivity of the plasma is strongly anisotropic. The conductive heat flux in this limit becomes

$$\mathbf{Q}_{\text{cond}} = -\kappa_e \hat{\mathbf{b}} (\hat{\mathbf{b}} \cdot \nabla T), \quad (3)$$

where  $\hat{\mathbf{b}} = \mathbf{B}/B$  is a unit vector in the direction of the magnetic field and  $\kappa_e$  is the thermal conductivity of free electrons (Braginskii 1965). While  $\kappa_e$  depends sensitively on temperature (Spitzer 1962), we take it to be constant in our calculations to simplify the interpretation of our results. This approximation does not affect our conclusions, because the physics of the buoyancy instabilities is independent of the conductivity in the limit that the thermal diffusion time across the spatial scales of interest is short compared to the dynamical time.

### 2.2 The Physics of Buoyancy Instabilities in Dilute Plasmas

The dissipative term in equation (1d) shows that fluid displacements in a plasma are not in general adiabatic. The standard analysis of buoyancy instabilities therefore does not apply, and the convective and mixing properties of a conducting plasma can be very different from those of an adiabatic fluid. In this paper, we focus on the limit in which thermal conduction is much faster than the dynamical time in the plasma. This applies on scales  $\lesssim 7(\lambda H)^{1/2}$ , where  $\lambda$  is the electron mean free path and  $H$  is the plasma scale height; this “rapid conduction limit” encompasses most scales of interest for the ICM. In this limit, the magnitude of the temperature gradient and the local orientation of the magnetic field control the convective stability of the plasma (Balbus 2000; Quataert 2008).

Although a single dispersion relation describes the linear stability of plasmas in this limit, it is easiest to understand the physics by separately considering cases where the temperature increases or decreases with height. Balbus (2000) first considered the case where the temperature decreases with height and identified the magnetothermal instability, or MTI. We show a schematic of this instability in the top row of Figure 1. The first panel of this figure shows a

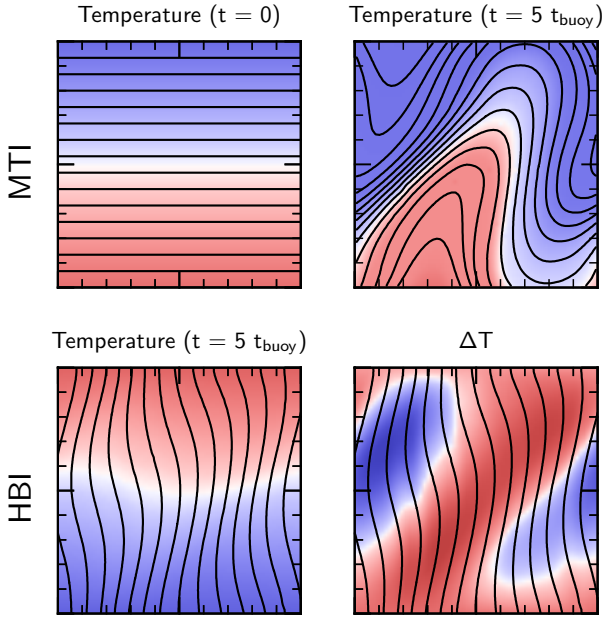


**Figure 1.** Illustration of the linear development of buoyancy instabilities in dilute plasmas from two-dimensional numerical simulations. Color shows the temperature, increasing from blue to red, while black lines trace the magnetic field. **Top Row:** Quasi-linear evolution of the MTI. *Left panel:* Initial equilibrium state, with  $\hat{b}_z = 0$  and the conductive heat flux  $\mathbf{Q} = 0$  everywhere. *Right panel:* The plasma at  $t = 5 t_{\text{buoy}}$  given an initial perturbation with  $\mathbf{k} = 2\pi/L \hat{\mathbf{x}}$ . Flux freezing and rapid conduction along field lines ensure that Lagrangian fluid displacements are nearly isothermal. If the initial state has a positive temperature gradient, upwardly displaced fluid elements are warmer than their surroundings; they will expand and continue to rise. Similarly, downwardly displaced fluid elements are cooler than their surroundings and will sink. **Bottom Row:** Quasi-linear evolution of the HBI. The initial equilibrium state has  $\hat{b}_z = 1$  and a net downward conductive heat flux, with  $\nabla \cdot \mathbf{Q} = 0$  everywhere. *Left panel:* The plasma at  $t = 5 t_{\text{buoy}}$  given an initial perturbation with  $k_x = k_z$ . The perturbation alters the geometry of the magnetic field, so that field lines are not parallel and there can be conductive heating and cooling of the plasma. *Right panel:* Temperature difference at  $t = 5 t_{\text{buoy}}$  relative to the initial condition. Magnetic field lines converge in upwardly displaced fluid elements, leading to an increased temperature. These fluid elements will then expand and continue to rise. Similarly, downwardly displaced fluid elements are conductively cooled, contract and continue to sink.

plasma in hydrostatic and thermal equilibrium, with a weak horizontal magnetic field. We apply a small, plane wave perturbation and, as the plasma evolves, the field lines follow the fluid displacements. Efficient conduction along these field lines keeps the displacements isothermal. Since the temperature falls with height, upwardly displaced fluid elements are warmer than their new surroundings; they expand and continue to rise. Similarly, downwardly displaced fluid elements sink. An order of magnitude calculation shows that displace-

ments grow exponentially, with the growth rate (or e-folding rate)  $p \sim |g \partial \ln T / \partial z|^{-1/2}$ .

Quataert (2008) investigated the limit in which the temperature of the plasma increases with height. The instability in this case is known as the heat-flux-driven buoyancy instability, or HBI. We sketch the growth of the HBI in the bottom row of Figure 1. Here, the initial equilibrium state has vertical magnetic field lines and a constant heat flux; the latter is required for the plasma to be in thermal equilibrium. However, perturbations to the magnetic field divert the heat flux and conductively heat or cool pockets of the plasma. If the temperature increases with height, upwardly displaced fluid elements become warmer than their surroundings and therefore experience a destabilizing buoyant response. These perturbations grow with the same growth rate  $|g \partial \ln T / \partial z|^{-1/2}$ .

Quataert (2008) performed a WKB analysis on equations (1a)–(1d) in the Boussinesq limit and obtained the following dispersion relation for plasma in a constant gravitational field  $\mathbf{g} = -g \hat{\mathbf{z}}$ , threaded by a constant magnetic field with any orientation in the  $\hat{\mathbf{x}} - \hat{\mathbf{z}}$  plane:

$$(p^2 + \omega_A^2)(p + \omega_\kappa) + p N^2(1 - \hat{k}_z^2) = \omega_\kappa \left( g \frac{\partial \ln T}{\partial z} \right) \left[ (2\hat{b}_z^2 - 1)(1 - \hat{k}_z^2) - 2\hat{b}_x \hat{b}_z \hat{k}_x \hat{k}_z \right]. \quad (4)$$

Here,  $p = -i\omega$  is the local growth rate of the mode (the time dependence of the perturbation is  $e^{pt}$ ),  $\omega_A = \mathbf{k} \cdot \mathbf{v}_A$  is the Alfvén crossing frequency,

$$N^2 = \frac{\gamma - 1}{\gamma} \frac{\mu m_H}{k_B} g \frac{\partial s}{\partial z} \quad (5)$$

describes the buoyant response of an adiabatic plasma,  $\hat{\mathbf{k}} = \mathbf{k}/k$  is the direction of the wave vector, and

$$\omega_\kappa = \frac{\gamma - 1}{\gamma} \frac{\kappa_e T}{P} (\hat{\mathbf{b}} \cdot \mathbf{k})^2 \quad (6)$$

is inversely proportional to the conduction time across the wavelength of the mode. It is convenient to identify  $\omega_{\text{buoy}} = |g \partial \ln T / \partial z|^{1/2}$  as a characteristic frequency for the buoyancy instabilities and we will also use  $t_{\text{buoy}} = \omega_{\text{buoy}}^{-1}$  and  $t_{\text{ad}} = N^{-1}$  in our analysis.

In the limit that conduction is rapid compared to any dynamical response ( $\omega_\kappa \gg \omega_A$ ,  $N$ ,  $\omega_{\text{buoy}}$ ), equation (4) simplifies to<sup>1</sup>

$$(p^2 + \omega_A^2) = \text{sgn}(\partial T / \partial z) \omega_{\text{buoy}}^2 \times \left[ (2\hat{b}_z^2 - 1)(1 - \hat{k}_z^2) - 2\hat{b}_x \hat{b}_z \hat{k}_x \hat{k}_z \right]. \quad (7)$$

As we stated in section 2.1, the growth rate in the rapid conduction limit is independent of the thermal conductivity.

Equation (7) shows that magnetic tension can suppress the MTI and HBI; if  $\omega_A^2 > \omega_{\text{buoy}}^2$ ,  $p^2$  must be negative, and the plasma is stable to small perturbations. In this paper, we focus on the relatively weak field limit in which magnetic

<sup>1</sup> In going from the cubic equation (4) to the quadratic (7), we have ignored a solution for  $p$ . This solution is exponentially damped on the conduction timescale and is not relevant to our analysis.

tension does not suppress the instabilities, and we take  $\omega_A \ll \omega_{\text{buoy}}$  in equation (7). The dominant role of the magnetic field in our analysis is to enforce anisotropic electron heat transport.

For any magnetic field direction  $\hat{\mathbf{b}}$ , the term in square brackets in equation (7) can be positive or negative; thus, there are always linearly unstable modes, irrespective of the thermal state of the plasma (excluding the singular case of  $\partial T/\partial z = 0$ ).

We finally note that, although we neglected cooling in equation (1d), it adds a term to equation (7) which is insignificant when the cooling time is much longer than  $\omega_\kappa^{-1}$  (Balbus & Reynolds 2008, 2010). This is not necessarily the case near the centers of cool-core clusters, and we plan to explore the combined effects of cooling and buoyancy instabilities in future work. For now, we assume that the buoyancy instabilities develop independently of cooling; this allows us to understand the nonlinear development and saturation of the instabilities themselves and therefore to assess their possible implications for the thermal balance of the plasma.

### 3 NUMERICAL METHOD

#### 3.1 Problem Setup and Integration

We consider the evolution of a volume of plasma initially in hydrostatic and thermal equilibrium, but subject to either the HBI or MTI. We seed our simulations with Gaussian-random velocity perturbations with a flat spatial power spectrum and a standard deviation of  $10^{-4} c_s$ . The small amplitude of these initial perturbations ensures that the instabilities start out in a linear phase and permits us to compare our results with the predictions of equation (7). Astrophysical perturbations are unlikely to be this subsonic, however, and the instabilities in our simulations take much longer to saturate than one would expect from the larger perturbations found in a more realistic scenario. We return to this point in section 6.

We highlight the distinctness of the HBI and MTI from adiabatic convection by choosing initial conditions with  $\partial s/\partial z > 0$  whenever possible, so that the plasma would be absolutely stable if it were adiabatic. Our results do not rely critically on this choice, however, because the plasma is not adiabatic and its evolution is independent of its entropy gradient to lowest order in  $\omega_{\text{buoy}}/\omega_\kappa$ . Our results are much easier to interpret when  $\omega_{\text{buoy}}$  doesn't vary across the simulation domain, and we prioritize this constraint on the initial condition over the sign of its entropy gradient (as we discuss in more detail below).

We solve equations (1a)–(1c), along with a conservative form of equation (1d), using the conservative MHD code *Athena* (Gardiner & Stone 2008; Stone et al. 2008) with the anisotropic conduction algorithm described in Parrish & Stone (2005) and Sharma & Hammett (2007). In particular, we use the monotonized central difference limiter on transverse heat fluxes to ensure stability. This conduction algorithm is sub-cycled with respect to the main integrator with a time step  $\Delta t \propto (\Delta x)^2$ ; our simulations are therefore

more computationally expensive than adiabatic MHD calculations. We draw most of our conclusions from simulations performed on uniform Cartesian grids of  $(64)^3$  and  $(128)^3$ . We also performed a large number of two-dimensional simulations on grids of  $(64)^2$ ,  $(128)^2$  and  $(256)^2$ . We found that the kinetic energy generated in our local HBI simulations converges by a resolution of  $(64)^3$ ; our global HBI simulations require roughly 60 grid cells per scale height to give a converged kinetic energy. The MTI is somewhat more sensitive to resolution; we tested the convergence of these simulations by comparing the results of an identical simulation performed at  $(128)^3$  and  $(256)^3$ .

We perform our calculations in the plane-parallel approximation with uniform gravity  $\mathbf{g} = -g\hat{\mathbf{z}}$ . We fix the temperature at the upper and lower boundaries of our computational domain, and we extrapolate the pressure into the upper and lower ghost cells to ensure that hydrostatic equilibrium holds at the boundary. For all other plasma variables, we apply reflecting boundary conditions in the direction parallel to gravity and periodic boundary conditions in the orthogonal directions. As we discuss in section 4, the choice of fixed temperatures at the upper and lower boundaries has an important effect on the non-linear evolution. Simulations with Neumann boundary conditions in which the temperature at the boundaries is free to adjust would give somewhat different results (see, e.g., Parrish & Stone 2005). Our choice of Dirichlet boundary conditions is largely motivated by the fact that many galaxy clusters in the local universe are observed to have non-negligible temperature gradients (Piffaretti et al. 2005).

We perform both local (with the size of the simulation domain  $L$  much smaller than the scale height  $H$ ) and global ( $L \gtrsim H$ ) simulations of the MTI and HBI. The local simulations separate the development of the instability from any large-scale response of the plasma, allowing us to study the dynamics in great detail. However, because the response of the plasma on larger scales can influence the nonlinear evolution and saturation of the instabilities, we also carry out global simulations.

#### 3.2 Local Simulations

In sections 3–5, we work in units with  $k_B = \mu m_p = 1$ . As noted previously, we restrict our analysis to plasmas with rapid conduction; we find that setting  $\kappa_e = 10 \times \rho \omega_{\text{buoy}} L^2$  puts our local simulations safely in this limit. This corresponds to a thermal diffusion time across the box of  $\sim 0.1 \omega_{\text{buoy}}^{-1}$ . We initialize our local HBI simulations with a linear temperature gradient:

$$T(z) = T_0 (1 + z/H), \quad (8a)$$

$$\rho(z) = \rho_0 (1 + z/H)^{-3}, \quad (8b)$$

$$P(z) = \rho(z) T(z). \quad (8c)$$

We choose to set  $\rho_0 = 1$  and  $g = 1 = 2 T_0/H$ . Unless otherwise noted, we take  $H = 2$  ( $T_0 = 1$ ) in our local simulations

and we evolve a volume of plasma from  $z = 0$  to  $z = L = 0.1$ , i.e., over  $\sim 5\%$  of a scale-height.

We use the setup of Parrish & Stone (2005) for our local MTI simulations:

$$T(z) = T_0 (1 - z/H), \quad (9a)$$

$$\rho(z) = \rho_0 (1 - z/H)^2, \quad (9b)$$

$$P(z) = \rho(z) T(z), \quad (9c)$$

with  $g = 1$  and  $H = 3$ . The MTI induces large vertical displacements in the plasma, and our reflecting boundary conditions clearly influence its evolution; we attempt to minimize the effects of the boundaries by sandwiching the unstable volume of plasma between two buoyantly neutral layers. Parrish & Stone (2005) describe this setup in more detail.<sup>2</sup>

Both of the above atmospheres have positive entropy gradients and therefore would be stable in the absence of anisotropic conduction. The results we describe in this paper are entirely due to non-adiabatic processes.

We show in section 4.1 that local and global HBI simulations give very similar results; we therefore use the simpler, local simulations for most of our analysis of the HBI. By contrast, the large-scale vertical motions induced by the MTI make its evolution inherently global; as we describe in section 4.2, local simulations do not give a converged result independent of  $L/H$ . We therefore study the saturated state of the MTI using global simulations, which require an alternate set of initial conditions.

### 3.3 Global Simulations

The physical properties of the plasma in a global simulation can vary by an order of magnitude or more across the simulation domain. This complicates our study of the HBI and MTI because the instabilities can be in different stages of evolution at different spatial locations. Similarly, the kinetic and magnetic energies generated by the instabilities in a global simulation can be functions of height, obscuring their dependence on other parameters. While one must confront these problems when studying buoyancy instabilities in an astrophysical context, we avoid them by choosing initial conditions with a buoyancy time that is constant with height. We specify

$$g(z) = g_0 e^{-z/S}, \quad (10a)$$

$$T(z) = \exp \left[ \pm \frac{S\omega_{\text{buoy}}^2}{g_0} (e^{z/S} - 1) \right]. \quad (10b)$$

The positive and negative signs in equation (10b) produce atmospheres unstable to the HBI and MTI, respectively. Note that  $T(z=0) = 1$  as in our local simulations. We take  $g_0 = 1$ ,  $S = 3$  and  $\omega_{\text{buoy}}^2 = 1/2$  and numerically solve for  $\rho(z)$  so that the initial atmosphere is in hydrostatic equilibrium. The

atmosphere defined by equation (10b) does not have a single, well-defined scale height. We therefore define  $H$  so that  $L/H = \ln(T_{\text{max}}/T_{\text{min}})$ ; this definition for  $H$  is analogous to that used in our local simulations and  $L/H$  reflects the total free energy available to the instabilities. Because  $H$  is a defined, rather than fundamental, property of the atmosphere, it is not independent of the size of the simulation domain. We carry out simulations with domain sizes  $L = 0.5$  and  $2.0$ , which have  $L/H = 0.27$  and  $1.4$ , respectively.

Simulations with a larger simulation domain size inherently permit larger vertical displacements, and the boundary conditions do not influence the evolution of the plasma as strongly as they do in a local simulation. We find that the neutrally stable layers described in section 3.2 don't alter the results of our global simulations, and thus we do not include them in our setup.

We chose the conductivity in our local simulations so that  $\kappa_e = 10 \rho \omega_{\text{buoy}} L^2$ , but the corresponding constraint on the time step becomes impractical for our global simulations. Instead, we adjust  $\kappa_e$  so that the ratio  $\kappa_e/L$  is the same as it is in the local simulations. This keeps the ratio of the conduction time to the sound crossing time constant, and is appropriate if the turbulence driven by the MTI or HBI reaches a terminal speed less than or of order the sound speed. We carried out simulations with different values of the conductivity and verified that our results are insensitive to factor of few changes in  $\kappa_e$ .

The atmosphere we use for our global MTI simulations has a negative entropy gradient. One might worry that the results of these simulations—which aim to focus on the MTI—would be biased by the presence of adiabatic convection. This is, however, only a pedagogical inconvenience;  $\omega_\kappa > N$  on all relevant scales in the simulation, so the adiabatic limit to equation (4) is not important, and the evolution of the plasma is nearly independent of its entropy gradient. To confirm this we carried out  $L = 0.27 H$  simulations with both sets of initial conditions; they give very similar results. Additionally, we performed one simulation of adiabatic convection using this setup, and the behavior of this simulation is entirely different from the MTI, especially at late times.

### 3.4 Turbulence

The pure HBI/MTI simulations described in the previous sections are physically very instructive but astrophysically somewhat idealized. In order to better understand the astrophysical role of the HBI and MTI, we also study their interaction with other sources of turbulence and fluid motion. We assume that these take the form of isotropic turbulence; we include such turbulence via the externally imposed force field  $\mathbf{f}$  in equation (1b). Following Lemaster & Stone (2008), we compute  $\mathbf{f}$  in momentum space from scales  $k_0 = \{4, 6, 8\} \times 2\pi/L$ , down to  $k_{\text{max}} = 2 k_0$ , with an injected energy spectrum  $\dot{E}_k^{(\text{inj})} \propto k^{-3}$ . We then randomize the phases, perform a Helmholtz decomposition of the field, discard the compressive component, transform the field into configuration space, and normalize it to a specified energy injection

<sup>2</sup> Note that, although Parrish & Stone (2005) describe these extra layers as buoyantly stable, the effect of the isotropic conductivity is to make them buoyantly neutral.

**Table 1.** Parameters for the HBI simulations (§ 4.1).

Name	$D$	res	$L/H$	$\kappa$
h1	2	64	0.05	7.07
h2	3	64	0.05	7.07
h3	3	128	0.75	0.47
h4	3	128	1.40	0.35

All simulations are performed on square Cartesian grids of size  $L$ .  $D$  is the dimensionality of the simulation, res is the number of grid cells along a side, and  $\kappa$  is the conductivity (in units of  $k_B/\mu m \times \rho \omega_{\text{buoy}} L^2$ ). All of these simulations are local (eq. 8), except for the one with  $L/H = 1.4$ , which uses the global setup (eq. 10). We initialized all of these simulations with weak horizontal magnetic fields ( $B/\sqrt{4\pi} = 10^{-6}$ ).

rate. We find that the turbulence sets up a nonlinear cascade that is not very sensitive to either the driving scale or the injected spectrum of the turbulence.

This prescription for turbulence is statistically uniform in both space and time and therefore provides a controlled environment in which to study the interaction between turbulence and buoyancy instabilities. This may not, however, be a good approximation to real astrophysical turbulence; we discuss the implications of our choice in sections 5 and 6.

## 4 NONLINEAR SATURATION

### 4.1 Saturation of the HBI

Parrish & Quataert (2008) described the nonlinear saturation of the HBI, but they did not explicitly test the dependence of their results on the size of the computational domain. This dependence turns out to be crucial for the MTI (see § 4.2), but we show here that the size of the domain has little effect on the saturation of the HBI. Nonetheless, we describe the nonlinear behavior of the HBI in reasonable detail, expanding on the physical interpretation given in previous papers (although our HBI results do not differ significantly from those of previous authors). The saturation of the HBI is the simplest process we consider in this paper and serves as a useful comparison for our new results.

We study the saturation of the HBI using 2D and 3D simulations spanning a range of domain sizes  $L/H$ . Table 1 lists all of the simulations presented in this section.

Figure 2 shows snapshots of the evolution of temperature and magnetic field lines in a local, 2D HBI simulation. We chose this simulation to simplify the field-line visualization, but the results in Figure 2 apply equally to our local and global 3D simulations. We initialized this simulation in an unstable equilibrium state with vertical magnetic field lines ( $\hat{b}_z = 1$ ). As described in section 3.1, we seed this initial condition with small velocity perturbations; the HBI causes these perturbations to grow in the first three panels of Figure 2. The evolution becomes nonlinear in the third panel, when the velocity perturbations reach  $\sim 4\%$  of the sound

speed. Afterwards, the instability begins to saturate and the plasma slowly settles into a new equilibrium state. The last panel in Figure 2 shows that this saturated state is highly anisotropic: the magnetic field lines are almost entirely orthogonal to gravity. Flux conservation implies that the fluid motions must also be anisotropic, with most of the kinetic energy in horizontal motions at late times (see Fig. 3, discussed below). These horizontal motions are very subsonic: in all of our simulations, the velocities generated by the HBI are significantly less than 1% of the sound speed in the saturated state.

Because the fluid velocities remain small, the linear dispersion relation (eq. 7) captures much of the evolution of the HBI, even at late times. For any magnetic field orientation, the fastest growing modes are the ones with  $\mathbf{k}$  along the axis  $\hat{\mathbf{b}} \times (\hat{\mathbf{b}} \times \mathbf{g})$ ; these modes have the growth rate

$$p_{\text{max}} = |\omega_{\text{buoy}} \hat{b}_z|, \quad (11)$$

which decreases as the field lines become horizontal. Additionally, when  $\hat{b}_z^2 < 1/2$ , only modes with  $\hat{k}_z^2 > 1 - 4(\hat{b}_z^2 - \hat{b}_z^4)$  are unstable. Since the HBI saturates by making the field lines horizontal ( $\hat{b}_z \rightarrow 0$ ), both the maximum growth rate of the instability and the volume of phase space for unstable modes decrease as the HBI develops. This strongly limits the growth of the perturbations, and helps explain why the instability saturates relatively quiescently.

As argued by Parrish & Quataert (2008), the HBI saturates when its maximum growth rate  $p_{\text{max}}$  vanishes, so that there are no longer unstable modes. While this is clearly a sufficient condition for the plasma to reach a new stable equilibrium, it is by no means necessary: the instability could, e.g., saturate via nonlinear effects, but in practice this is not the case (at least for simulations without an additional source of turbulence). Equation (11) for  $p_{\text{max}}$  shows that the HBI could saturate by making either  $\partial T/\partial z$  or  $\hat{b}_z$  vanish; intuitively, the HBI is powered by a conductive heat flux, which it must extinguish in order to stop growing. Erasing the temperature gradient might seem like the more natural saturation channel, since the conduction time across the domain is much shorter than the time it takes the HBI to develop and saturate. In an astrophysical setting, however, the large-scale temperature field is often controlled by cooling, accretion or other processes apart from the HBI. We therefore impose the overall temperature gradient in our simulations by fixing the temperature at the top and bottom of the domain, so that  $\omega_{\text{buoy}}$  is roughly independent of time and saturation requires  $\hat{b}_z = 0$ .

Since the HBI saturates by making the magnetic field lines horizontal, we take the  $\hat{b}_z \rightarrow 0$  limit in equation (7) to understand the late-time behavior of the plasma:

$$\omega = \pm \omega_{\text{buoy}} (1 - \hat{k}_z^2)^{1/2}. \quad (12)$$

We have assumed here that the magnetic field is weak enough for magnetic tension to be negligible on the scales of interest.<sup>3</sup> Equation (12) shows that the saturated state of the HBI

<sup>3</sup> Note that equation 12 only strictly applies when the magnetic

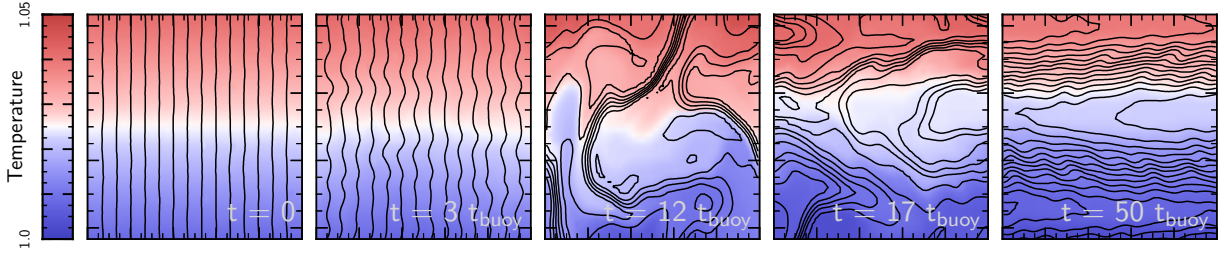


**Figure 2.** Evolution of the HBI with an initially vertical magnetic field in a local, 2D simulation (simulation h1 in Table 1). Color shows temperature and black lines show magnetic field lines. A small velocity perturbation to the initial state seeds exponentially growing modes which dramatically reorient the magnetic field to be predominantly horizontal. The induced velocities are always highly subsonic and, after  $t \sim 20 t_{\text{buoy}}$ , are also almost entirely horizontal. Once the plasma reaches its saturated state, it is buoyantly stable to vertical displacements. The plasma does not resist horizontal displacements, but the saturated state is nearly symmetric to these displacements and they do not change its character.

is buoyantly stable, but that there is a family modes with  $\hat{k}_z = 1$  which feel no restoring force. This simply reflects the fact that the plasma is stably stratified and resists vertical displacements. Displacements orthogonal to gravity are unaffected by buoyancy, however, and appear as zero-frequency modes in the dispersion relation.

Figure 3 demonstrates this asymmetry between vertical and horizontal displacements in the late time evolution of the plasma. This figure shows the kinetic energy in horizontal and vertical motions as a function of time. During the initial, linear growth of the instability ( $t \lesssim 10 t_{\text{buoy}}$ ), buoyantly unstable fluid elements accelerate toward the stable equilibrium, and the kinetic energy is approximately evenly split among vertical and horizontal motions. As the instability saturates, however, the plasma becomes buoyantly stable and traps the vertical motions in decaying oscillations (internal gravity waves). The horizontal motions keep going, however, and retain their kinetic energy for the duration of the simulation. This difference in the response of the plasma to vertical and horizontal motions accounts for the anisotropy of the velocity field in the saturated state of the HBI.

Figure 4 shows the evolution of the rms magnetic field angle (left panel) and magnetic energy (right panel) in 3D HBI simulations for three different values of the size of the computational domain  $L$  relative to the scale height  $H$ . The zero frequency modes discussed above also dominate the evolution of the magnetic field at late times, after the motions become nonlinear ( $t \gtrsim 10 t_{\text{buoy}}$ ). The horizontal displacements stretch out the field lines, amplifying and reorienting them. Quantitatively, we expect that  $\hat{b}_z \sim \lambda/\xi \propto t^{-1}$ , where  $\lambda$  is a characteristic scale for the modes in the saturated state,  $\xi$  is the magnitude of the horizontal displacements, and we have assumed that the velocity is constant with time. The left panel of Figure 4 shows that the dependence in the sim-

ulations is quite close to this, with  $\hat{b}_z \propto t^{-0.85}$ .<sup>4</sup> Stretching the field lines in this manner amplifies the field strength by an amount  $\delta B \propto \xi$ ; if the velocity is constant with time, we expect  $B^2 \propto t^2$ . The right panel of Figure 4 shows that this time dependence is approximately true for our two larger HBI simulations; the amplification is slightly slower in the very local calculation with  $L/H = 0.05$ . There is no indication that the magnetic field amplification has saturated at late times in the HBI simulations. We suspect that the amplification would continue until the magnetic and kinetic energy densities reach approximate equipartition, but we would have to run the simulation for a very long time to verify this.

One of the important results in Figure 4 is that the saturated state of the HBI is nearly independent of the size of the computational domain  $L/H$ . Since the late time evolution of the plasma is driven only by horizontal displacements, the key dynamics all occur at approximately the same height in the atmosphere. The saturation of the HBI is thus essentially local in nature and should not be sensitive to the global thermal state of the plasma or the details of the computational setup.

The dramatic reorienting of the magnetic field caused by the HBI severely suppresses the conductive heat flux through the plasma. The conductive flux is proportional to  $\langle \hat{b}_z^2 \rangle$ , which decreases in time  $\propto (t/t_{\text{buoy}})^{-1.7}$ . The saturated state of the HBI is also buoyantly stable and resists any vertical mixing of the plasma. As a result, the convective energy fluxes in our HBI simulations are very small,  $\sim 10^{-6} \rho c_s^3$ . The effect of the HBI therefore is to strongly insulate the plasma against both conductive and convective energy transport. This can dramatically affect the thermal evolution of the plasma (Parrish et al. 2009; Bogdanović et al. 2009).

The fact that the growth rate of the HBI depends on the local orientation of the magnetic field, as well as the thermal structure of the plasma, makes it very different from adiabatic

field is *exactly* horizontal. More generally, there will still be unstable modes with growth rate given by equation 11; this growth rate is very slow in the saturated state of the HBI, however, and these modes don't change the dynamics of the plasma.

<sup>4</sup> The slight difference relative to the simple predictions of flux freezing given the velocity field in Figure 3 may be due to the finite resolution of our simulations, which prevents us from resolving the field line direction when  $\hat{b}_z \lesssim 10 \times dz/L$ .



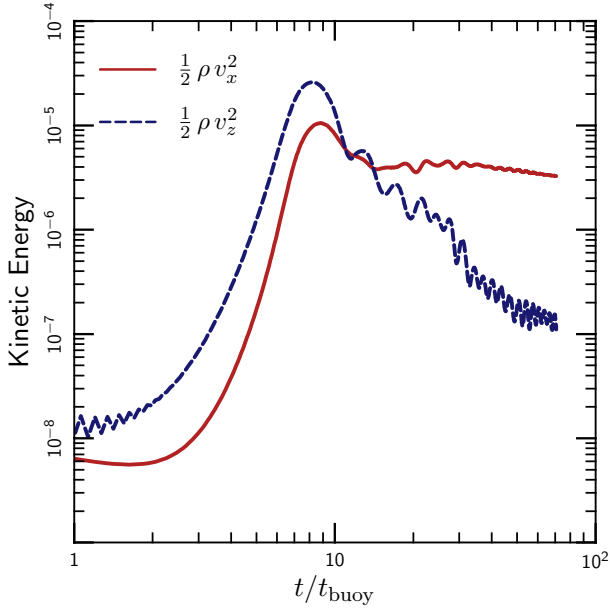


**Figure 3.** Evolution of the vertical and horizontal kinetic energy in a local, 2D HBI simulation (simulation h1 in Table 1). The units are such that the thermal pressure  $P \approx 1$  and the initial magnetic energy is  $B^2/8\pi = 10^{-12}$ . After a period of exponential growth in which the  $x$  and  $z$  motions are in approximate equipartition, the HBI saturates and the kinetic energy ceases to grow. At this point, the energy in the vertical motion is in the form of stable oscillations, which decay non-linearly. The horizontal motions are unhindered, however, and persist for the entire duration of the simulation. These horizontal motions are responsible for the asymmetry of the magnetic field shown in Figure 4.

convection. This dependence on the magnetic field structure provides a saturation channel in which the kinetic energies are very small compared to the thermal energy (e.g., in Fig. 3,  $\rho v^2/nkT \sim 10^{-5}$ ). Critically, these highly subsonic motions occur in simulations in which the boundary conditions allow for the presence of a sustained, order unity, temperature gradient ( $d \ln T/d \ln z \sim 1$ ). In an adiabatic simulation, the analogous sustained entropy gradient would generate convective motions with  $\rho v^2 \sim nkT$ . This does not occur in an HBI-unstable plasma. Thus, although a plasma with a positive temperature gradient is in general buoyantly unstable, the effect of the HBI is to peacefully stabilize the plasma within a few buoyancy times by suppressing the conductive heat flux through the plasma. The resulting, stably-stratified plasma then resists vertical mixing and, in the absence of strong external forcing, we expect the fluid velocities and magnetic field lines to be primarily horizontal. In section 5, we perturb this state with externally driven, isotropic turbulence and test the strength of the stabilizing force.

#### 4.2 Saturation of the MTI

Figure 5 shows the evolution of one of our local, 2D MTI simulations. As in the HBI simulation shown in Figure 2, we

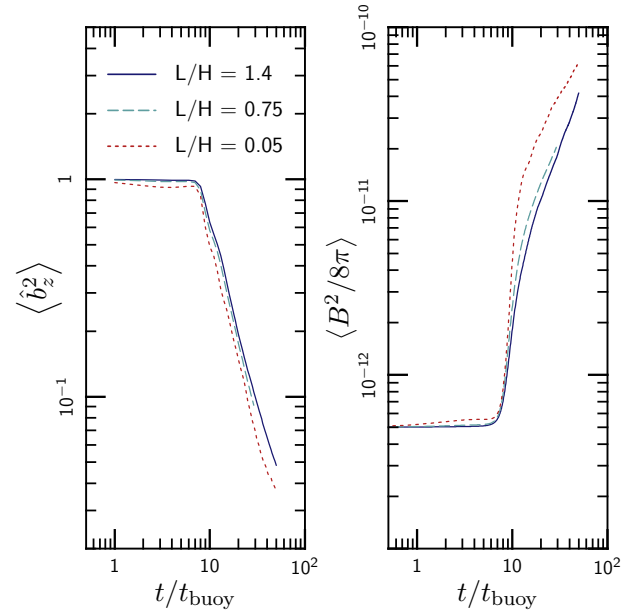


**Figure 4.** Evolution of the orientation (left) and energy (right) of the magnetic field in 3D HBI simulations for three different values of the size of simulation domain relative to the temperature scale-height ( $L/H$ ) (simulations h2–h4 in Table 1). Units are such that the thermal pressure  $P \approx 1$ . The results are nearly independent of size of the simulation domain. As described in § 4.1, the HBI saturates by shutting itself off; the linear exponential growth ends at  $t \sim 10 t_{\text{buoy}}$ , and most of the evolution of the magnetic field happens afterward. This evolution is driven by the horizontal motions shown in Figure 3, which both amplify and reorient the magnetic field. After a brief period of exponential growth, the field amplification is roughly linear in time. By contrast, the field amplification by the MTI is exponential in time (see Fig. 8).

initialized this simulation in an unstable equilibrium state (a weak horizontal magnetic field) and seeded it with the small velocity perturbations described in section 3.1. The MTI and HBI stem from very similar physics, and as a result have very similar linear dynamics. The nonlinear behavior of the two instabilities is entirely different, however. While the HBI saturates relatively quiescently by driving the plasma to a buoyantly stable and highly anisotropic state, the MTI generates vigorous, sustained convection that tends to isotropize both the magnetic and velocity fields.

As we did for the HBI, we study the saturation of the MTI using 2D and 3D simulations spanning a range of domain sizes  $L/H$ . Table 2 summarizes the simulations presented in this section.

Since the linear dispersion relation successfully describes the nonlinear evolution and saturation of the HBI, it is a good place to begin our discussion of the MTI. The MTI is described by equation (7) when  $\partial T/\partial z < 0$ . The linear evolution of the MTI is the opposite of that of the HBI: the MTI operates when the temperature decreases with height, its fastest growing modes are the ones with wave vectors  $\mathbf{k}$  parallel to  $\hat{\mathbf{b}}$ , and the force that destabilizes the MTI is exactly that which



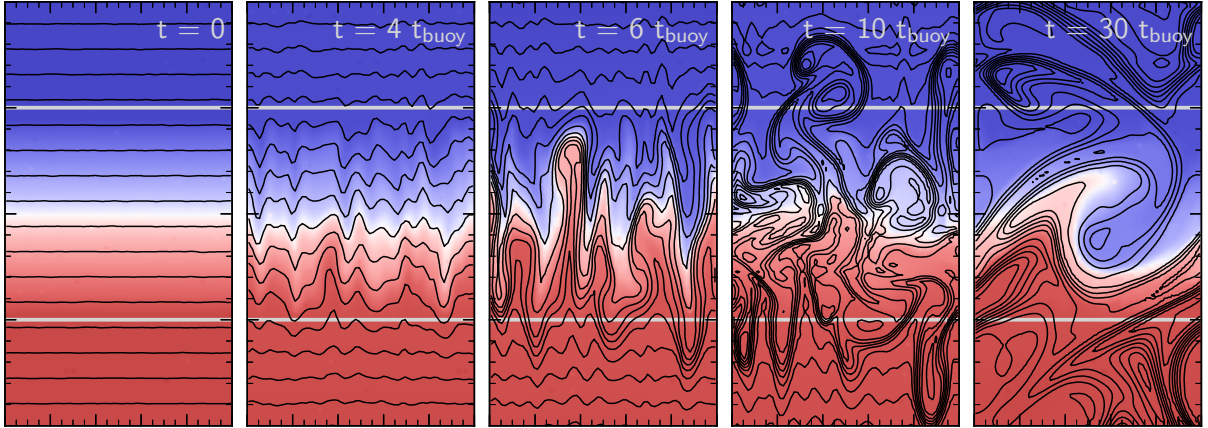


**Figure 5.** Evolution of the MTI with an initially horizontal magnetic field in a local, 2D simulation (simulation m1 in Table 2). Gray horizontal lines show the transition to the buoyantly neutral layers described in § 3.2; the color scale is identical to that in Figure 2. Initial perturbations grow by the mechanism described in § 2.2 (Fig. 1); rising and sinking plumes rake out the field lines until, by  $t = 6 t_{\text{buoy}}$ , they are mostly vertical. This configuration is, however, nonlinearly unstable to horizontal displacements, which generate a horizontal magnetic field and thus continually seed the MTI (see Fig. 6). The result is vigorous, sustained convection in marked contrast to the saturation of the HBI in Fig. 2. In this local simulation, buoyant plumes accelerate until they reach the neutrally stable layers. The boundaries prematurely stop the growth of the MTI, and the local simulation under predicts the kinetic energy generated by the MTI (see Fig. 7).

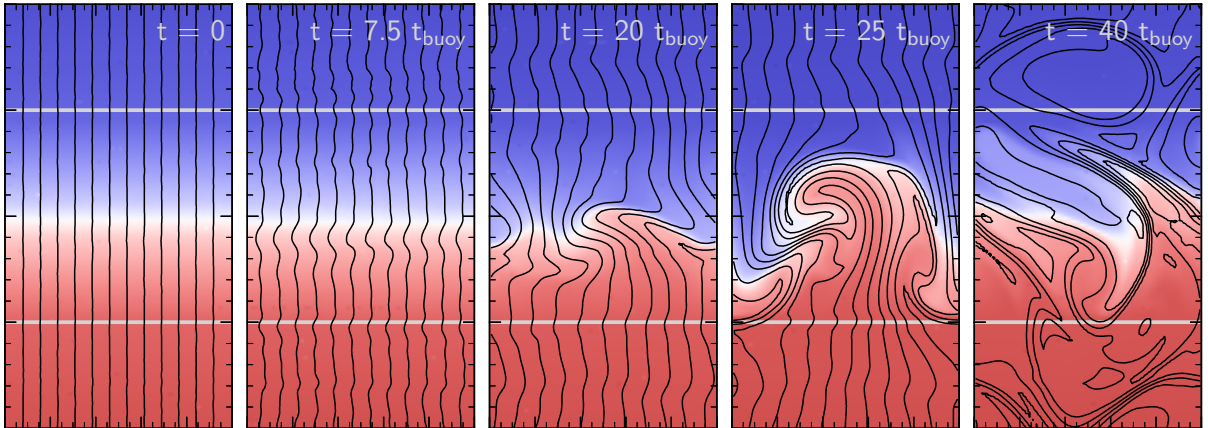


**Figure 6.** Evolution of the MTI in a plasma with an initially vertical magnetic field in a local, 2D simulation (simulation m2 in Table 2). This configuration is linearly stable according to equation (7), but there are zero-frequency,  $k_x = 0$ , modes which do not have a restoring force. Physically, these correspond to horizontal motions which do not feel gravity/buoyancy. Because of this zero frequency mode, small random initial perturbations add a horizontal component to the magnetic field, eventually rendering the plasma unstable to the MTI. This creates a feedback loop, allowing the MTI to generate vigorous, sustained convection; the HBI does not have this same feedback loop and so does not generate sustained turbulence (Fig. 2). At late times, the results of this simulation with an initially vertical magnetic field are very similar to Figure 5 which starts with a horizontal magnetic field.

stabilizes the HBI in its saturated state. Equation (7) shows that the maximum growth rate of the MTI goes to zero when  $\hat{b}_z = 1$ . By analogy with the HBI, it thus seems reasonable to expect that the MTI also saturates quiescently, by making the field lines vertical.

The first three panels of Figure 5 show that this is nearly what happens. As the perturbations grow exponentially, the buoyantly rising and sinking blobs rake out the field lines, making them largely vertical. The growth rate of the MTI goes to zero when the field lines become vertical;

since the velocities are still small at this point in the evolution ( $\sim 10^{-2} c_s$ ), one might expect the MTI to operate like the HBI and quiescently settle into this stable equilibrium state. Instead, however, the MTI drives sustained turbulence for as long as the temperature gradient persists. The plasma never becomes buoyantly stable, and the magnetic field and fluid velocities are nearly isotropic at late times.

We can understand this evolution using the same approach we employed for the HBI. Although the plasma in our MTI simulations never reaches a state in which the MTI

**Table 2.** Parameters for the MTI simulations (§ 4.2).

Name	$D$	res	$L/H$	$\kappa$	Field Configuration
m1	2	64	0.033	7.07	horizontal
m2	2	64	0.033	7.07	vertical
m3	3	64	0.033	7.07	horizontal
m4	3	64	0.033	7.07	vertical
m5*	3	128	0.500	0.31	horizontal
m6*	3	128	1.400	0.35	horizontal

The definitions of  $L$ ,  $D$ , and  $\kappa$  are the same as in Table 1. All simulations use the local setup (eq. 9), except for the one with  $L/H = 1.4$ , which is global (eq. 10). Each of these simulations was initialized with a weak magnetic field  $B/\sqrt{4\pi} = 10^{-4}$  with the orientation indicated in the table. \*We also repeated simulations m5 and m6 with initial field strengths  $B/\sqrt{4\pi} = 10^{-4}, 0.0014, 0.0245$

growth rate is zero, examining the properties of this state is very instructive. The equilibrium state of the MTI with  $\hat{b}_z = 1$  (i.e., a vertical field) has precisely the same dispersion relation as the saturated state of the HBI, given by equation (12). There are again zero frequency (neutrally stable) modes of the dispersion relation which correspond to horizontal perturbations to the equilibrium state of the MTI; these experience no restoring force, because the restoring force is buoyant in nature and unaffected by horizontal displacements.<sup>5</sup> Critically, however, these zero frequency perturbations now add a horizontal component to the magnetic field, pulling the plasma out of the equilibrium state and rendering it unstable to the MTI.

Figure 6 vividly illustrates this process. This figure shows a simulation that starts with the linearly *stable* equilibrium state of the MTI (a vertical magnetic field), seeded with the same highly subsonic velocity perturbations as before. The compressive component of the perturbation rapidly damps because the Mach number is small, and buoyancy traps the vertical components of the perturbation in small-amplitude oscillations, as predicted by equation (12). The incompressive, horizontal displacements propagate freely, however, and by  $t = 7.5 t_{\text{buoy}}$ , they have noticeably changed the local orientation of the magnetic field. The plasma is no longer in its stable equilibrium state, and by  $t = 20 t_{\text{buoy}}$ , it is clear that this process has excited the MTI. At late times, the simulations initialized with horizontal (linearly unstable; Fig. 5) and vertical (linearly stable; Fig. 6) magnetic fields are qualitatively indistinguishable. Thus, although equation (7) shows that a

<sup>5</sup> This conclusion is more subtle than the analogous argument for the HBI, because the equilibrium state has a nonzero heat flux. If the horizontal displacements aren't incompressive, the field lines could pinch together, heating and destabilizing parts of the plasma. These perturbations do not appear in eq (12) because we have taken the Boussinesq limit. It is in principle possible that such compressive perturbations contribute to destabilizing the  $\hat{b}_z = 1$  MTI state in our simulations, but all of our analysis is consistent with the neutrally stable zero frequency perturbations being the critical ingredient.

plasma with  $\partial T/\partial z < 0$  is linearly stable if the magnetic field is vertical, that configuration is nonlinearly unstable.

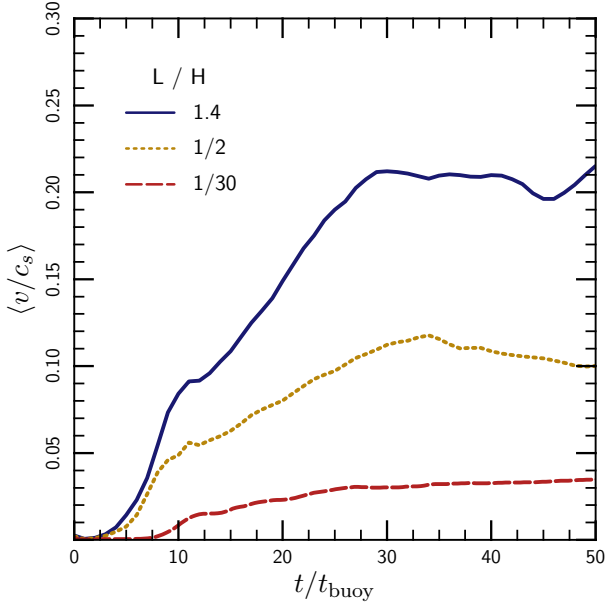
The nonlinear instability of the  $\hat{b}_z = 1$  state of the MTI precludes the magnetic saturation channel. The zero frequency horizontal motions generate a horizontal magnetic field component from the vertical magnetic field, seeding the instability and closing the dynamo loop. This continuously drives the MTI and generates sustained turbulence. Without a linear means to saturate, the MTI grows until nonlinear effects can compete with the linear instability, which requires  $v \sim c_s$ .

Figure 7 shows the Mach number in 3D MTI simulations as a function of time, for different sizes of the computational domain  $L/H$ . The MTI buoyantly accelerates rising or sinking fluid elements. For simulations with  $L \ll H$ , the velocities generated by the MTI are artificially suppressed because the small size of the computational domain prematurely stops the buoyant acceleration (Fig. 5); the results in this Figure 7 are reasonably consistent with mixing length estimate of  $v \sim \sqrt{L}$ . By contrast, for simulations with  $L \gtrsim H$ , the Mach numbers approach  $\sim 1$  so that the MTI taps into the full buoyant force associated with the unstable temperature gradient. This is only true, of course, because our boundary conditions fix the temperature at the top and bottom of the computational domain. If the temperatures were free to vary, the MTI could saturate by making the plasma isothermal. Which of these saturation mechanisms is realized in a given astrophysical system will depend on the heating and cooling mechanisms that regulate the temperature profile of the plasma.

Figure 8 shows the evolution of the magnetic field orientation (left panel) and energy (right panel) as a function of time in our 3D MTI simulations (for two different values of  $L/H$ ). The sustained, vigorous turbulence generated by the MTI in the nonlinear regime ( $t \gtrsim 10 t_{\text{buoy}}$ ) rapidly amplifies the magnetic field. The magnetic and kinetic energies reach approximate equipartition in our simulations, with  $B^2/8\pi \sim 0.1 \rho v^2$ . The kinetic and magnetic energies generated by the MTI together contribute  $\sim 5\text{--}10\%$  of the pressure support in its saturated state.

The evolution of the magnetic field geometry, shown in the left panel of Figure 8, nicely illustrates the transition of the MTI from the linear to nonlinear regime. During the linear phase of the instability ( $t \lesssim 10 t_{\text{buoy}}$ ), the plasma accelerates toward the equilibrium state with  $\hat{b}_z = 1$ . After the evolution becomes nonlinear ( $t \gtrsim 10 t_{\text{buoy}}$ ), however, the MTI drives sustained turbulence, which nearly isotropizes the magnetic field.

While the HBI works to insulate the plasma against vertical energy transport, the MTI enhances it. Figure 8 shows that the conductive flux through the plasma is slightly greater than  $\sim 1/3$  of the field free value  $\kappa_e \nabla T$  (because  $\langle \hat{b}_z^2 \rangle \sim 0.4$ ). Moreover, the MTI leads to large fluid velocities and correlated temperature and velocity perturbations—hot pockets of plasma rise, while cool pockets sink. These imply that the MTI drives an efficient outwards convective heat flux. Figure 9 shows that this flux can be  $\sim 1.5\%$  of  $\rho c_s^3$ , consistent with the Mach numbers of  $\sim 0.2$  in Figure 7. This convective



**Figure 7.** Volume-averaged Mach numbers of the turbulence generated by the MTI in 3D simulations, for three different values of the size of simulation domain relative to the temperature scale-height  $L/H$ . The MTI buoyantly accelerates the unstable fluid elements; if the size of the simulation domain is smaller than a scale-height, the boundaries suppress the growth of the instability. Local simulations with  $L/H = 1/30$  therefore strongly under predict the strength of the turbulence generated by the MTI. In global simulations with  $L \gtrsim H$ , the MTI leads to turbulence with average Mach numbers of  $\sim 0.2$ ; the velocity distribution extends up to  $\sim 5$  times the mean.

flux is probably not large enough to influence the thermodynamics of the ICM, but it could be important in other environments where the MTI can operate, such as the interiors of white dwarfs and neutron stars (Chang et al. 2010).

## 5 INTERACTION WITH OTHER SOURCES OF TURBULENCE

Thus far, we have described the development and saturation of buoyancy instabilities only in the idealized case of an otherwise quiescent plasma. In a more astrophysically realistic scenario, however, other processes and sources of turbulence may also act on the plasma and the resulting dynamics can be more complicated. For example, the evolution of the HBI won't simply proceed until the growth rate is everywhere zero. Instead, we expect the saturated state to involve a statistical balance among the various forces; this balance depends on the buoyant properties of the plasma and provides a test of our understanding of the nonlinear behavior of the HBI and MTI. Furthermore, any change in the saturated state of the plasma due to the interaction between the HBI/MTI and other sources of turbulence could change the astrophysical implications of these instabilities.

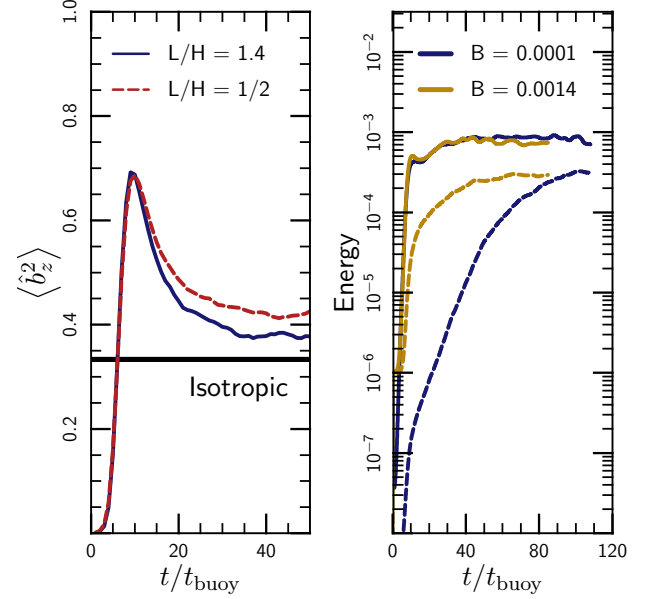


**Figure 8.** **Left panel:** Evolution of the magnetic field orientation in 3D MTI simulations, for two different values of the size of simulation domain relative to the temperature scale-height  $L/H$ . During the linear phase of evolution ( $t \lesssim 10 t_{\text{buoy}}$ ), the MTI drives the plasma toward a nearly vertical magnetic field, i.e.,  $\hat{b}_z \sim 1$ . When the instability becomes nonlinear, however, (near  $t \sim 10 t_{\text{buoy}}$ ) the evolution changes. Unlike the HBI, the plasma never settles into an equilibrium state; instead the MTI drives vigorous turbulence. This turbulence amplifies and nearly isotropizes the magnetic field. **Right panel:** Evolution of the magnetic (dashed line) and kinetic (solid line) energy in local ( $L/H = 1/2$ ) 3D MTI simulations, with different initial field strengths. These local simulations have a positive entropy gradient, but under-predict the magnetic and kinetic energy produced by the MTI. The magnetic energy in the saturated state approaches  $\sim 10\% \times \rho v^2$ .

We choose to explore the interaction between buoyancy instabilities and other sources of turbulence using the idealized, isotropic turbulence model described in section 3.4. While this model glosses over the details of what generates the turbulence, we hope that it captures the essential physics of the problem, allowing us to study the effect of turbulence without unnecessarily restricting our analysis to specific applications. We intend to specialize to specific sources of turbulence in future work, but our present analysis should apply in the ICM, accretion disks, and anywhere else the assumptions summarized in section 2.2 apply.

In order to characterize the turbulence, we define a timescale for it to influence the plasma. We define this “distortion time” in terms of the spatial velocity spectrum:  $t_{\text{dist}}(\ell) = \ell/\delta v(\ell)$ , where

$$\delta v(\ell) \equiv \left[ \int (\delta \mathbf{v}(\mathbf{k}))^2 \delta(|\mathbf{k}| - 2\pi/\ell) \frac{d^3 k}{(2\pi)^3} \right]^{1/2}, \quad (13)$$

and  $\delta v(\mathbf{k})$  is the Fourier transform of the velocity field. We expect the relevant parameter describing the importance of

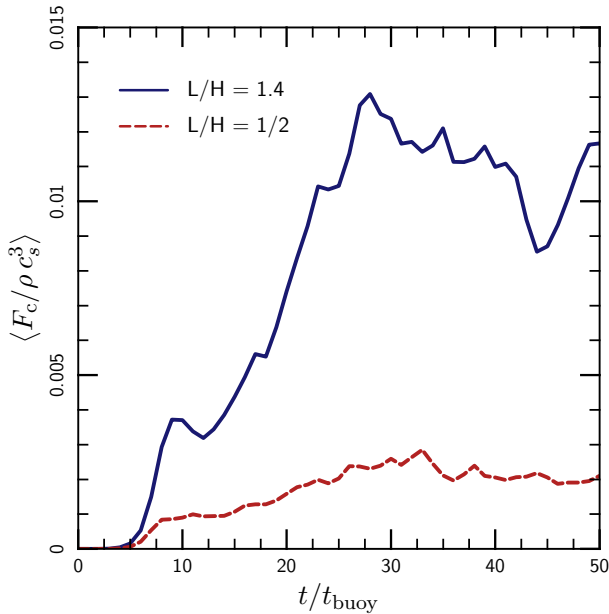


**Figure 9.** Convective energy fluxes generated by the MTI. The large turbulent velocities associated with the MTI (Fig. 7) lead to efficient convective transport of energy, at a reasonable fraction of the maximal value,  $\rho c_s^3$ . In these MTI simulations, the conductive energy flux is  $\sim 0.4$  times the field-free value and always dominates the convective energy flux for galaxy cluster conditions.

the turbulence to be the ratio of the timescales  $t_{\text{buoy}}/t_{\text{dist}}$ . This represents a dimensionless strength of the turbulence; if  $t_{\text{buoy}}/t_{\text{dist}} \gtrsim 1$ , the turbulence displaces fluid elements faster than buoyancy can restore them, and we expect the velocities and magnetic field lines to become isotropic. In the opposite limit, buoyancy still plays an important role in the evolution of the plasma. The scale dependence of the distortion time makes the ratio  $t_{\text{buoy}}/t_{\text{dist}}$  a function of scale. We define this ratio at the scale where the velocity spectrum of the injected turbulence peaks. This is roughly consistent with the driving scale of the turbulence and typically represents the scale with the most energy.

In the following sections, we study the transition from a state dominated by buoyancy to one dominated by isotropic turbulence using a number of simulations of the HBI and MTI, with turbulence in the range  $0.1 \lesssim t_{\text{buoy}}/t_{\text{dist}} \lesssim 10$ .

### 5.1 Effect of Turbulence on the HBI

Figure 10 shows representative snapshots of the temperature and magnetic field lines in saturated states of our HBI simulations with turbulence; the strength of the injected turbulence increases from the top left panel through the bottom right (the labels correspond to the values of  $t_{\text{buoy}}/t_{\text{dist}}$ ). When  $t_{\text{dist}}$  is long compared to the buoyancy time, as in the first panel of Figure 10, the turbulence is weak; the HBI therefore dominates and the evolution of the plasma is similar to that described in section 4.1. This saturated state of the HBI feels

**Table 3.** Parameter study for the HBI simulations with turbulence (§ 5.1).

$D$ (2)	res (64)	$L$ (0.1)	$H$ (2.0)	$B_0$ ( $10^{-6}$ )	$\tilde{k}_0$
—	—	—	—	—	2
—	—	—	1.0	—	2
—	—	—	3.0	—	2
—	—	—	—	—	4
—	—	1.0	—	—	4
—	—	0.3	—	—	4
3	—	—	—	—	4
3	—	—	—	$10^{-3}$	4
3	—	1.0	—	$3 \times 10^{-4}$	4
3	128	1.0	—	$3 \times 10^{-4}$	4
—	—	—	—	—	6
—	—	—	—	—	8
—	256	—	—	—	8
3	—	—	—	—	8

The simulations were initialized with our local setup (eq. 8) and an initial magnetic field strength  $B_0$ . Each simulation was performed on uniform Cartesian grids of side  $L$ , resolution res and dimension  $D$ . We varied the size of the simulation domain  $L$  (scaling the conductivity as described in § 3.3), the plasma scale height  $H$  and the initial magnetic field strength  $B_0$ ; the fiducial values for these parameters are included in the table header (— indicates the fiducial value). For each entry in the table, we performed simulations with both initially horizontal and vertical magnetic fields. As described in the § 5.1, these simulations include isotropic turbulence injected at the scale  $k_0 = 2\pi/L \times \tilde{k}_0$  and with a range of turbulent energy injection rates to give  $0.1 \lesssim t_{\text{buoy}}/t_{\text{dist}} \lesssim 10$ .

a buoyant restoring force which resists vertical displacements  $\xi_z$  with a force per unit mass  $f_{\text{buoy}} = \omega_{\text{buoy}}^2 \xi_z$ . As we increase the strength of the applied turbulence in the following panels of Figure 10, the vertical displacements grow, and the field deviates more strongly from the  $\hat{b}_z = 0$  equilibrium state of the HBI. When  $t_{\text{dist}}$  is short compared to the buoyancy time, as in the last panel of Figure 10, turbulence can displace the fluid elements faster than buoyancy can restore them. The turbulence then dominates the evolution of the plasma, tangling and isotropizing the field lines.

Figure 10 also shows the length-scale dependence of the transition from an HBI to a turbulence dominated state. It is clear in the second and third panels that the HBI has globally rearranged the field lines, but that the turbulence is increasingly efficient at smaller scales. This is a consequence of the fact that turbulence typically perturbs the plasma in a scale-dependent way, while the buoyant restoring force of the HBI does not. If the turbulence follows a Kolmogorov cascade, the force  $\sim \omega^2/k \propto k^{1/3}$  increases with decreasing scale, so the turbulence will always win on sufficiently small length-scales. It is therefore somewhat ambiguous whether turbulence or the HBI dominates a certain configuration, as the answer will typically depend on scale. As mentioned earlier, we skirt this issue by defining  $t_{\text{dist}}$  at the scale where the velocity spectrum of the injected turbulence peaks. When assessing the astro-

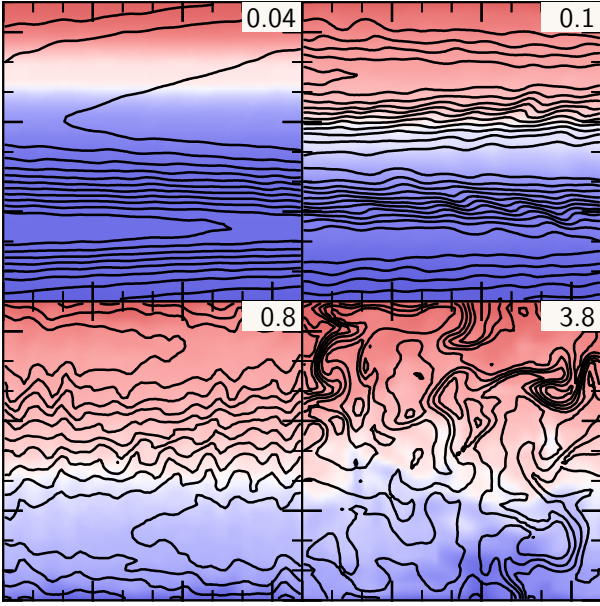


**Figure 10.** Snapshots of the saturated states of our 2D HBI simulations with externally driven turbulence. Colors show the temperature (increasing from blue to red), and black lines show magnetic field lines. Each panel is labeled with the dimensionless strength of the turbulence in the simulation,  $t_{\text{buoy}}/t_{\text{dist}}$ , defined in § 5. When  $t_{\text{buoy}} \lesssim t_{\text{dist}}$ , as in the top two panels, the HBI dominates the evolution of the plasma. When  $t_{\text{buoy}} \gtrsim t_{\text{dist}}$ , the turbulence can isotropize the magnetic field, but it does so in a scale-dependent way with the large scales retaining memory of the horizontal field imposed by the HBI.

physical importance of the HBI, it is important to keep this scale in mind. If the scale where the turbulent energy spectrum peaks is smaller than the temperature gradient length scale, the HBI may still insulate the plasma against conduction, even if the field lines are isotropized on smaller scales.

In order to quantify the transition from an HBI-dominated configuration to one dominated by turbulence, we measure the mean orientation of the magnetic field via the volume average of  $\hat{b}_z^2$ . The saturated value for this quantity approaches zero when the HBI dominates, and  $1/D$  when the magnetic field is isotropic, where  $D$  is the number of dimensions in the simulation.

Figure 11 shows the saturated field angle as a function  $t_{\text{buoy}}/t_{\text{dist}}$ . The points in this figure represent simulations with different driving scales  $k_0$ , different dimensionality, and different buoyancy times  $t_{\text{buoy}}$  (Table 3 summarizes our parameter study). Symmetry of the coordinate axes requires that  $b_z^2 = 1/2$  in 2D or  $1/3$  in 3D if the magnetic field is isotropic. To include both our 2D and 3D simulations on the same plot, we shift our 3D values of  $\langle b_z^2 \rangle$  by a factor of  $3/2$ . To within the scatter shown in Figure 11, we find that the saturated value of  $\langle b_z^2 \rangle$  depends only on the ratio  $t_{\text{buoy}}/t_{\text{dist}}$ : for  $t_{\text{buoy}} \gtrsim t_{\text{dist}}$  the turbulence is strong and the field becomes relatively isotropic while for  $t_{\text{buoy}} \lesssim t_{\text{dist}}$  the isotropic turbulence is weak and the HBI drives the magnetic field to become relatively hori-

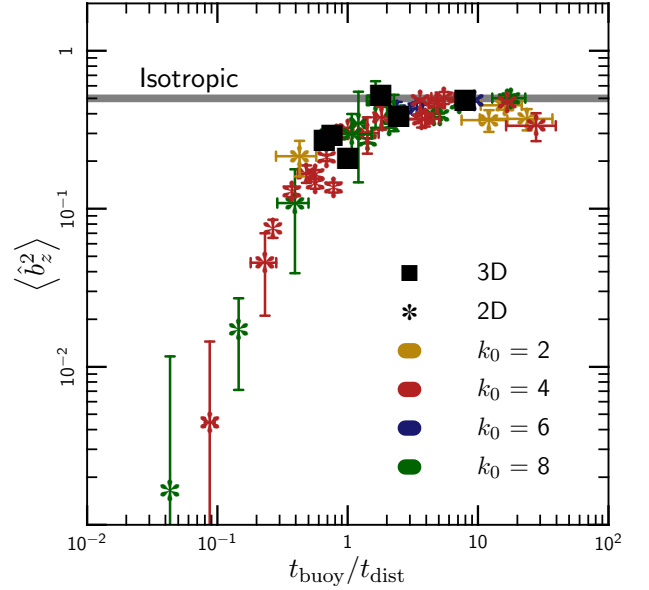


**Figure 11.** Saturated magnetic field orientation as a function of the strength of the externally driven turbulence,  $t_{\text{buoy}}/t_{\text{dist}}$ , for local HBI unstable atmospheres with  $t_{\text{buoy}} = 1, \sqrt{2}$  and  $\sqrt{3}$ . The thick gray line is an isotropic magnetic field in 2D. Colored points represent simulations with turbulence driven on different scales. Squares mark 3D calculations; the values of  $\langle b_z^2 \rangle$  for the 3D simulations have been shifted by a factor  $3/2$  since isotropy implies  $b_z^2 = 1/2$  in 2D but  $b_z^2 = 1/3$  in 3D. Error bars represent  $1\sigma$  statistical fluctuations in  $b_z$  and  $t_{\text{dist}}$ .

zontal. The fact that the transition between these two states occurs around  $t_{\text{buoy}} \sim t_{\text{dist}}$  suggests that our definition of  $t_{\text{dist}}$ , though somewhat arbitrary, is reasonable.

The bulk of the simulations in Figure 11 are 2D, and we do not have any 3D simulations in the very weak turbulence limit. These simulations are computationally expensive, both because of conduction and because we have to run for a long time for turbulence and the HBI to reach a statistical steady state; using 2D simulations allowed us to explore a larger fraction of the interesting parameter space. While the development of turbulence is very different in two and three dimensions, the HBI is essentially two-dimensional in nature. Moreover, the key dynamics governing the interaction between the HBI and the turbulence are dominated by the energy-containing scale of the turbulence—the precise power-spectrum of the fluctuations (which differs in 2D and 3D) is less critical. Scaling for dimension, we find that the saturated states of our 2D and 3D simulations are nearly identical. We thus believe that results in Figure 11 in the weak turbulence limit are a good description of the magnetic field structure in 3D systems as well.

These results on the interaction between the HBI and other sources of turbulence support an analogy between the saturated state of the HBI and ordinary, adiabatic stable stratification. The most important effect of the HBI in the saturated states of our simulations is to inhibit mixing in the



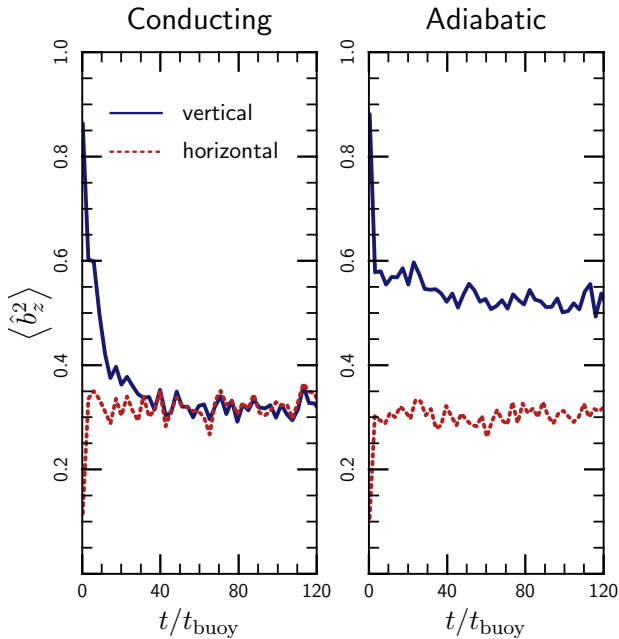


**Figure 12.** Magnetic field orientation as a function of time in 2D simulations with turbulence and the HBI for different initial magnetic field orientations;  $t_{\text{buoy}}/t_{\text{dist}} = 0.8$ . *Left panel:* Simulations with anisotropic thermal conduction. *Right panel:* Adiabatic simulations with no conduction (and thus no HBI). Different curves represent simulations with initially vertical and horizontal magnetic field lines, respectively. Conducting simulations eventually reach the same saturated state independent of the initial magnetic field direction. Adiabatic simulations are very similar to the conducting ones if the field is initially horizontal, highlighting the fact that in the saturated state of the HBI the plasma is buoyantly stable and behaves dynamically like an adiabatic fluid.

direction of gravity. Ordinary stable stratification also inhibits vertical mixing and, as suggested by Sharma et al. (2009b), our parameter  $t_{\text{buoy}}/t_{\text{dist}}$  is analogous to the Richardson number used in the hydrodynamics literature. To further expand on this analogy, Figure 12 shows a comparison of anisotropically conducting (left panel) and adiabatic (right panel) simulations with equal values of  $t_{\text{buoy}}/t_{\text{dist}}$ . For the adiabatic simulations, we define  $t_{\text{buoy}} = t_{\text{ad}}$ , i.e., using the entropy gradient rather than the temperature gradient. The left panel of Figure 12 shows simulations with the same injected turbulence, but initialized with vertical or horizontal magnetic field lines. In these simulations, the saturated state is independent of the initial condition. That is, the interaction between turbulence and the HBI leads to a well defined magnetic field orientation that is independent of the initial field direction.

By contrast, in the adiabatic simulations (right panel of Fig. 12), the final magnetic field orientation depends on the initial field direction. For an initially vertical field in an adiabatic plasma, the turbulence slowly isotropizes the magnetic field direction. However, the adiabatic simulations with initially horizontal field lines reach a saturated state that is very similar to that of the HBI simulations. In the adiabatic simu-

lations, the magnetic field is essentially passive, but it traces the fluid displacements. The stable stratification competes with the turbulence and sets a typical scale for vertical displacements in the saturated state. This scale, in turn, determines the magnetic field geometry. The magnetic field plays no dynamical role in this process. The fact that the anisotropically conducting simulations reach the same statistical steady state highlights that the saturated state of the HBI behaves dynamically very much like an adiabatic, stably stratified, plasma.

## 5.2 Effect of Turbulence on the MTI

To complete our analysis, we study how externally imposed isotropic turbulence affects the saturation of the MTI. Figure 13 shows the volume averaged magnetic field orientation as a function of time in MTI simulations with additional turbulence, for different values of the strength of the turbulence  $t_{\text{buoy}}/t_{\text{dist}}$ . These are local simulations (with domain sizes  $L/H = 0.5$ ; initialized using eq. (9)) which have the pedagogical advantage of a positive entropy gradient, but which under-predict the kinetic energy generated by the MTI. We drive the turbulence at relatively small scales ( $kL/2\pi = 8$ ) so that subsonic turbulence can still satisfy  $t_{\text{buoy}}/t_{\text{dist}} > 1$ . Both our driven turbulence and the MTI tend to isotropize the magnetic field, so it is not a priori clear whether the field orientation is a good indication of the importance of turbulence relative to the MTI. Although Figure 13 shows that there is no strong dependence of the saturated field orientation on the strength of the turbulence, the time dependence of the field orientation clearly shows the effects of the turbulence on the MTI.

In general, the evolution of the MTI proceeds through two stages: there is a linear phase, where the plasma accelerates toward its nominal stable state (which has a vertical magnetic field), and a nonlinear transition to the saturated state, where the strong turbulence generated by the MTI isotropizes the velocities and field lines. In the absence of additional turbulence, the linear phase is characterized by field lines that are primarily in the direction of gravity (Fig. 5). Figure 13 shows that additional sources of strong (rapidly shearing) turbulence suppress this linear phase of the MTI. Indeed, the evolution of the field angle with time in our strongest turbulence simulations ( $t_{\text{buoy}}/t_{\text{dist}} = 4.7$ ) is quite similar to what we find in simulations of an adiabatic plasma in which the MTI is not present.

It would, however, be incorrect to conclude from Figure 13 that the MTI is unimportant if there are other strong sources of turbulence in the plasma. The fundamental reason for this is that the growth of the MTI does not depend significantly on scale, while the effects of the other sources of turbulence do. Figure 14 shows velocity spectra for the simulations in Figure 13; for comparison we also show the velocity spectra in adiabatic simulations, which correspond to the power spectra produced solely by the injected turbulence. Figure 13 demonstrates that even in simulations with very strong imposed turbulence ( $t_{\text{buoy}}/t_{\text{dist}} = 4.7$ ) there is still

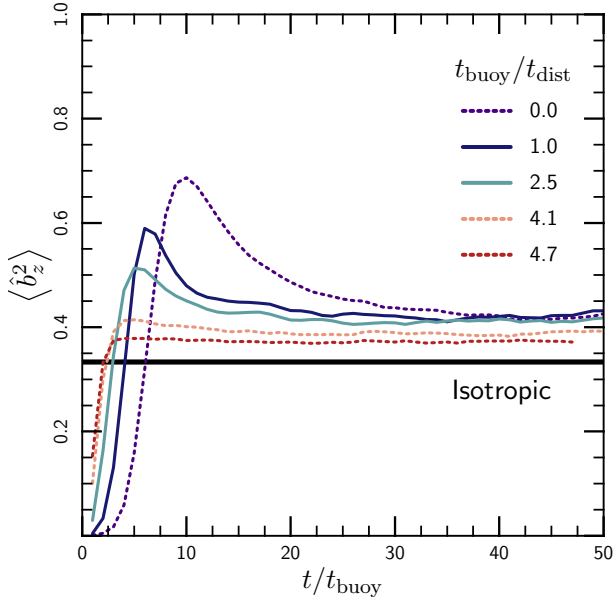


**Figure 13.** Magnetic field orientation as a function of time in 3D simulations with turbulence and the MTI, for different values of the strength of the turbulence  $t_{\text{buoy}}/t_{\text{dist}}$ . In all of the simulations, the magnetic field is relatively isotropic in the saturated state. However, the early-time ‘overshoot’ towards a vertical magnetic field due to the MTI is suppressed in the presence of strong turbulence with  $t_{\text{buoy}} \gtrsim t_{\text{dist}}$ . These relatively local simulations ( $L = 0.5H$ ) underestimate the kinetic energy generated by the MTI (Fig. 7) and therefore the strength of the turbulence required to influence it.

significant excess power on the largest scales in the computational domain ( $kL/2\pi \lesssim 10$ ). This large-scale power is due to the MTI. Moreover, the turbulent energy due to the MTI dominates the total turbulent kinetic energy in the plasma. These results highlight that ‘strong’ turbulence is a scale-dependent statement. Suppressing the MTI requires having  $t_{\text{buoy}}/t_{\text{dist}} \gg 1$  on *all scales*, up to the temperature/pressure scale-height of the plasma. Because the MTI itself generates nearly sonic velocities, this suppression would require close to supersonic turbulence. In practice, it is therefore unlikely that additional sources of turbulence can fully suppress the MTI in most astrophysical environments where it is likely to occur (e.g., accretion disks and galaxy clusters).

## 6 DISCUSSION

The motion of electrons along, but not across, magnetic field lines in dilute, magnetized plasmas produces efficient, anisotropic transport of heat. Such plasmas are therefore non-adiabatic, and the standard analysis of buoyancy (or convective) instabilities does not necessarily apply. Quantitatively, conduction plays an essential role on scales less than  $7(\lambda H)^{1/2}$ , where  $\lambda$  is the electron mean free path and  $H$  is the plasma scale height. In this “rapid conduction limit,” the temperature gradient, rather than the entropy gradient, dictates

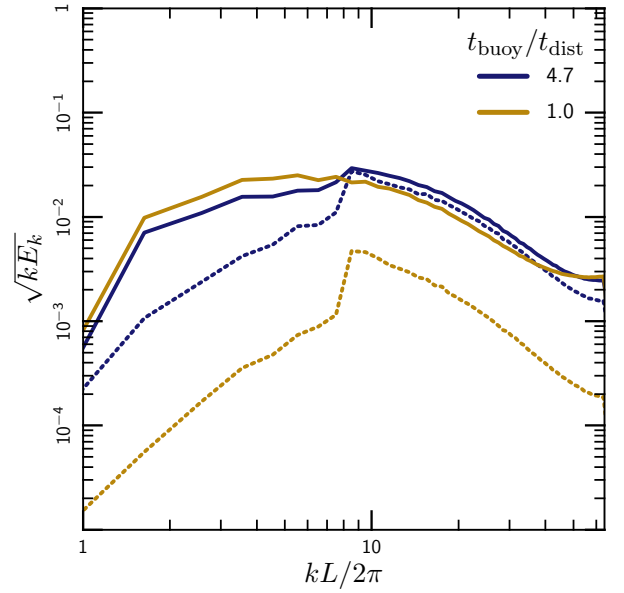


**Figure 14.** Velocity spectra in simulations with turbulence and the MTI (solid lines), for different values of the strength of the injected turbulence  $t_{\text{buoy}}/t_{\text{dist}}$ . The turbulence is driven at  $kL/2\pi = 8$ . For comparison, dashed lines show the power spectra in adiabatic simulations, in which the injected turbulence is the only source of power. Even when  $t_{\text{buoy}}/t_{\text{dist}} \gg 1$  at the driving scale of the turbulence, so that one might expect the MTI to be suppressed, the MTI produces significant turbulent energy on larger scales  $kL/2\pi \sim 2 - 10$ . Suppressing the MTI on all scales in a plasma would thus require  $t_{\text{buoy}}/t_{\text{dist}} \gg 1$  on all scales smaller than the scale-height.

the stability of the plasma, and the plasma is unstable for either sign of the temperature gradient (Balbus 2000; Quataert 2008). The convective instability in this limit is known as the HBI (MTI) when the temperature increases (decreases) with height.

Parrish & Stone (2005, 2007) and Parrish & Quataert (2008) extended the original linear analysis of the MTI and HBI into the nonlinear regime using numerical simulations. In this paper, we have reconsidered the nonlinear saturation of the HBI and MTI. Our work adds to previous investigations because we have identified a key difference between the two instabilities and are able to understand the nonlinear behavior of the MTI more completely. This paper therefore represents a significant change in our understanding of the possible astrophysical implications of the MTI (but not the HBI). We have also studied the effect of an external source of turbulence on both the MTI and HBI. We conclude that other sources of turbulence in a plasma can change the saturation of the HBI, but that it is much harder to disrupt the MTI. Below we summarize our results and discuss their astrophysical implications, focusing on the intracluster medium (ICM) of galaxy clusters.



### 6.1 HBI

The HBI occurs whenever the temperature increases with height in an anisotropically conducting plasma. Plasmas in the rapid conduction limit are in general linearly unstable, unless the magnetic field lines are horizontal (eq. 7). Horizontal field lines represent a fixed point in the evolution of the plasma: if the plasma somehow reaches such a state (and is not perturbed away by another process), it will remain there forever. A horizontal magnetic field is therefore a natural saturation channel for the HBI.

This “magnetic” saturation mechanism can be understood using the linear dispersion relation of the plasma (§ 4.1). Starting from a linearly unstable state, the HBI induces both horizontal and vertical motions in the plasma. As the HBI develops, however, the vertical motions become trapped in internal gravity waves. These waves decay, leaving only the horizontal motions at late times; thus, the fluid velocities are very anisotropic in the saturated state. Since the horizontal motions don’t incur a buoyant response, the horizontal displacements can be very large. These motions stretch out the magnetic field lines, amplifying and reorienting them, and drive the plasma towards its stable equilibrium with horizontal magnetic field lines. These horizontal motions therefore drive the nonlinear evolution and saturation of the HBI.

Since the saturation of the HBI is dominated by horizontal displacements, the key dynamics all occur at approximately the same height in the atmosphere. The saturation of the HBI is thus essentially local in nature. We have demonstrated this explicitly by carrying out simulations with different domain sizes relative to the plasma scale-height; the results of these simulations are very similar (Fig. 4).

The growth rate of the HBI decreases dramatically as the instability progresses. The HBI therefore saturates quiescently, and the velocities in the saturated state are very subsonic (Fig. 3). The saturation is driven by horizontal motions with nearly constant velocities, so the nonlinear magnetic field amplification is approximately linear, rather than exponential, with time. These findings are consistent with those of Parrish & Quataert (2008). We note that the HBI is very much unlike adiabatic convection, which can only saturate by changing the thermal state of the plasma and therefore generates vigorous turbulence. The key difference between the HBI and adiabatic convection is that the source of free energy for the HBI is a conductive heat flux through the plasma, not merely the existence of a temperature gradient. Since the heat flux can be suppressed by rearranging the magnetic field, the HBI has a magnetic saturation channel that is not available to adiabatic convection.

The astrophysical implications of the HBI follow immediately from the nature of its saturated state. By reorienting the magnetic field lines, the HBI dramatically reduces the conductive heat flux through the plasma. The HBI should operate in the innermost  $\sim 100$ – $200$  kpc in the intracluster medium of cool-core galaxy clusters, where the observed temperature increases outward. As noted in Parrish & Quataert (2008), this is precisely where the cooling time of the ICM is shorter

than its age; the HBI removes thermal conduction as a source of energy for the cores, potentially exacerbating the cooling flow problem (Parrish et al. 2009).

Our results demonstrate that the saturated state of the HBI is buoyantly stable. This may not seem surprising, because it is exactly what one would expect if the ICM were adiabatic. The ICM is not, however, adiabatic, and thermal conduction would render it buoyantly neutral to vertical displacements if the magnetic field lines were tangled. The saturated state of the HBI is buoyantly stable only because of the nearly horizontal magnetic field lines (that are perpendicular to the temperature gradient). The HBI therefore inhibits vertical mixing and allows for the existence of weakly damped internal gravity waves in the plasma.

Sharma et al. (2009b) noted that the stable stratification associated with the saturated state of the HBI competes with other sources of turbulence in a well-defined way. This competition can be understood using a modified Richardson number  $t_{\text{buoy}}/t_{\text{dist}}$ , where  $t_{\text{buoy}}$  is the timescale for the HBI to grow and  $t_{\text{dist}}$  is a characteristic “distortion time,” or “eddy turnover time,” of the turbulence. When  $t_{\text{buoy}} \gtrsim t_{\text{dist}}$ , the turbulence can isotropize the plasma and remove all traces of the HBI (Fig. 11). When  $t_{\text{buoy}} \lesssim t_{\text{dist}}$ , the saturated state of the plasma represents a statistical balance between turbulence and the HBI, with the magnetic field becoming more horizontal, and the plasma more HBI-dominated, for smaller values of  $t_{\text{buoy}}/t_{\text{dist}}$ . The strength of other sources of turbulence is therefore crucial for understanding the astrophysical implications of the HBI.

Figure 11 provides a very simple mapping between the properties of the turbulence and the magnetic field geometry in the plasma. Given the strength of the turbulence and the thermal state of the plasma, this figure provides a recipe for determining the mean geometry of the magnetic field, and therefore the effective conductivity of the plasma. This can be used to interpret observational results or to construct semi-analytic models of anisotropic conduction for use in cosmological simulations.

Turbulence in the ICM is currently poorly constrained, and thus it is difficult to determine precisely how important the HBI is for the evolution of clusters. Reasonable estimates suggest that  $t_{\text{buoy}}/t_{\text{dist}} \sim 1$ , but more detailed simulations of clusters are required to determine this ratio more precisely. Future observations of the ICM with space-based x-ray calorimeters will place observational constraints on the level of turbulence. In addition, Faraday rotation measurements of the ICM will measure the orientation of the magnetic fields in clusters and constrain the role of the HBI (Bogdanović et al. 2010) (Pfrommer & Dursi (2010) describe another mechanism to measure the magnetic orientation in the ICM). Even if the turbulence is strong ( $t_{\text{buoy}}/t_{\text{dist}} \gtrsim 1$ ), the driving scale and filling factor of the turbulence may allow the HBI to dominate on some scales or at some locations (see Fig. 10 and associated discussion in § 5.1). As suggested by Parrish et al. (2010) and Ruszkowski & Oh (2010), the interaction between turbulence and the HBI might be part of a feedback loop for the thermal evolution of the ICM.

## 6.2 MTI

The nonlinear evolution of the MTI is more complex than that of the HBI. Just like the HBI, the MTI has linearly stable equilibria, but they are transposed: the linearly stable equilibrium states of the MTI have vertical field lines. We have shown, however, that the linearly stable equilibrium states turn out to be nonlinearly unstable; i.e., they are unstable to perturbations with a finite amplitude. This nonlinear instability arises because neutrally buoyant, horizontal displacements add a horizontal component to the magnetic field. This takes the plasma out of its linearly stable state and re-seeds the instability (Fig. 6 and § 4.2). As a result, the linearly stable equilibrium states of the MTI do not represent fixed points in the evolution of the instability, and the MTI cannot saturate simply by reorienting the magnetic field.

This difference eliminates the quiescent, magnetic saturation channel for the MTI and dramatically changes its evolution. Without a linear means to saturate, the instability grows until nonlinear effects dominate, which occurs when  $v \sim c_s$ . Unlike the HBI, the MTI therefore drives strong turbulence and operates as an efficient magnetic dynamo, much more akin to adiabatic convection. The astrophysical implications of the MTI are therefore entirely different from those of the HBI. The kinetic and magnetic energy generated by the MTI can contribute a significant (up to ten percent) non-thermal pressure support to the plasma in the saturated state. This is consistent with observational constraints on non-thermal pressure support in the ICM near the virial radius (George et al. 2009). This non-thermal pressure support may have consequences for mass estimates of clusters, which often rely on the assumption of hydrostatic equilibrium with thermal pressure support. Note, in particular, that the MTI is predicted to be present at precisely the same radii ( $\gtrsim$  the scale radius) to which x-ray and SZ mass measurements are most sensitive.

Because the MTI operates by buoyantly accelerating fluid elements until they approach the sound speed, the results of numerical simulations of the MTI are sensitive to the size of the computational domain. The boundaries of the domain can artificially suppress this acceleration, and simulations with sizes smaller than a scale height under-predict the kinetic energy generated by the MTI (this was the case in the original MTI simulations of Parrish & Stone 2005, 2007). The nonlinear development of the MTI is therefore quite sensitive to the global thermal state of the plasma, and an understanding of the MTI requires more careful numerical simulations than are needed for the HBI.

The saturated state of the MTI corresponds to a largely isotropic magnetic field, with a slight but persistent vertical (or radial) bias; this bias is robust even in the presence of other sources of strong turbulence (Fig. 13). We find that the magnetic energy generated by the MTI saturates at about 30% of the kinetic energy (Fig. 8). However, it may be difficult to observationally distinguish the turbulence generated by the MTI from that generated by other processes.

The large velocities generated by the MTI, along with correlations between the temperature and velocity perturba-

tions, imply that the MTI drives a large convective heat flux,  $\sim 1.5\% \times \rho c_s^3$  (Fig. 9). While this convective flux is probably too small to alter the thermal evolution of the ICM, it could be important in higher density astrophysical plasmas, where the electron mean free path is smaller and conduction isn't as efficient.

While the MTI cannot saturate by reorienting the magnetic field, it can saturate by making the plasma isothermal. Simulations with Neumann boundary conditions in which the temperature at the boundaries is free to adjust find that this is the case; the atmosphere becomes isothermal before the MTI has a chance to develop (Parrish et al. 2008). We fixed the temperature at the top and bottom boundaries of our simulations; this is partially motivated by the fact that many galaxy clusters in the local universe are observed to have non-negligible temperature gradients.

Sharma et al. (2008) carried out numerical simulations of the MTI in spherical accretion flows and found nearly radial magnetic fields, with modest turbulence. This quasi-linear saturation of the MTI might seem to contradict the results presented in this paper. Note, however, that in the Bondi inflow studied by Sharma et al. (2008), the plasma undergoes at most  $\sim 5 - 10$  MTI growth times before flowing in. After 10 growth times, our simulations also show approximately radial field lines and modest turbulence (Fig. 8). Moreover, the simulations of Sharma et al. (2008) covered a very large dynamic range in radius and may have lacked the resolution to see the full nonlinear development of the MTI.

The MTI growth time in the outer parts of the ICM is about 1 Gyr. Although our typical MTI simulations take  $\sim 10 - 20$  growth times to saturate, this does not preclude the importance of the MTI in galaxy clusters. Figure 8 shows that there is a long, linear ramp-up phase where the instability grows from the tiny perturbations we apply to the nonlinear state. Astrophysical perturbations are unlikely to be this subsonic. Figure 13 shows that the MTI can saturate in  $\sim 2 - 5$  growth times when subjected to larger perturbations, suggesting that the MTI is likely to become nonlinear in the outer parts of clusters. Cosmological simulations will be required to fully understand the implications of the MTI for galaxy clusters.

## ACKNOWLEDGMENTS

Support for I. J. .P and P. S. was provided by NASA through Chandra Postdoctoral Fellowship grants PF7-80049 and PF8-90054 awarded by the Chandra X-Ray Center, which is operated by the Smithsonian Astrophysical Observatory for NASA under contract NAS8-03060. M.M. and EQ were supported in part by NASA Grant NNX10AC95G, NSF-DOE Grant PHY-0812811, and the David and Lucile Packard Foundation. Computing time was provided by the National Science Foundation through the Teragrid resources located at the National Center for Atmospheric Research and the Pittsburgh Supercomputing Center.

**REFERENCES**

- Balbus S. A., 2000, *ApJ*, 534, 420  
 Balbus S. A., Reynolds C. S., 2008, *ApJL*, 681, L65  
 Balbus S. A., Reynolds C. S., 2010, *ApJL*, 720, L97  
 Bogdanović T., Reynolds C., Massey R., 2010, *ArXiv e-prints astro-ph.CO/1005.2193*  
 Bogdanović T., Reynolds C. S., Balbus S. A., Parrish I. J., 2009, *ApJ*, 704, 211  
 Braginskii S. I., 1965, *Reviews of Plasma Physics*, 1, 205  
 Chang P., Strubbe L. E., Menou K., Quataert E., 2010, *MNRAS*, p. 1003  
 Gardiner T. A., Stone J. M., 2008, *Journal of Computational Physics*, 227, 4123  
 George M. R., Fabian A. C., Sanders J. S., Young A. J., Russell H. R., 2009, *MNRAS*, 395, 657  
 Johnson B. M., Quataert E., 2007, *ApJ*, 660, 1273  
 Lemaster M. N., Stone J. M., 2008, *ApJL*, 682, L97  
 Parrish I. J., Quataert E., 2008, *ApJL*, 677, L9  
 Parrish I. J., Quataert E., Sharma P., 2009, *ApJ*, 703, 96  
 Parrish I. J., Quataert E., Sharma P., 2010, *ApJL*, 712, L194  
 Parrish I. J., Stone J. M., 2005, *ApJ*, 633, 334  
 Parrish I. J., Stone J. M., 2007, *ApJ*, 664, 135  
 Parrish I. J., Stone J. M., Lemaster N., 2008, *ApJ*, 688, 905  
 Pfrommer C., Dursi J. L., 2010, *Nature Physics*, 6, 520  
 Piffaretti R., Jetzer P., Kaastra J. S., Tamura T., 2005, *A&A*, 433, 101  
 Quataert E., 2008, *ApJ*, 673, 758  
 Ruszkowski M., Oh S. P., 2010, *ApJ*, 713, 1332  
 Sharma P., Chandran B. D. G., Quataert E., Parrish I. J., 2009a, *ApJ*, 699, 348  
 Sharma P., Chandran B. D. G., Quataert E., Parrish I. J., 2009b, in S. Heinz & E. Wilcots ed., *American Institute of Physics Conference Series Vol. 1201 of American Institute of Physics Conference Series, Turbulence and Mixing in the Intracluster Medium*. pp 363–370  
 Sharma P., Hammett G. W., 2007, *Journal of Computational Physics*, 227, 123  
 Sharma P., Quataert E., Stone J. M., 2008, *MNRAS*, 389, 1815  
 Shcherbakov R. V., Baganoff F. K., 2010, *ApJ*, 716, 504  
 Spitzer L., 1962, *Physics of Fully Ionized Gases*  
 Stone J. M., Gardiner T. A., Teuben P., Hawley J. F., Simon J. B., 2008, *ApJS*, 178, 137